Topological Features in Time-Dependent Advection-Diffusion Flow

Filip Sadlo, Grzegorz K. Karch, and Thomas Ertl

Abstract Concepts from vector field topology have been successfully applied to a wide range of phenomena so far—typically to problems involving the transport of a quantity, such as in flow fields, or to problems concerning the instantaneous structure, such as in the case of electric fields. However, transport of quantities in time-dependent flows has so far been topologically analyzed in terms of advection only, restricting the approach to quantities that are solely governed by advection. Nevertheless, the majority of quantities transported in flows undergoes simultaneous diffusion, leading to advection-diffusion problems. By extending topology-based concepts with diffusion, we provide an approach for visualizing the mechanisms in advection-diffusion flow. This helps answering many typical questions in science and engineering that have so far not been amenable to adequate visualization. We exemplify the utility of our technique by applying it to simulation data of advection-diffusion problems from different fields.

1 Introduction

Vector field topology is a powerful tool for the analysis of vector fields, since it reveals their overall structure and provides insights into their intrinsic dynamics. In the visualization community, the problem of extracting topological features has been extensively researched for more than two decades. Visualization by traditional (stationary) 2D vector field topology builds on the concept of critical points which represent isolated zeros of the vector field, i.e., isolated points where velocity magnitude vanishes. By additionally extracting separatrices, i.e., sets of stream lines that converge to these points in forward or reverse time, one obtains the overall structure of a vector field, i.e., these sets of lines divide the domain into regions of qualitatively different behavior. Nevertheless, there arise some issues regarding the

---

Filip Sadlo, Grzegorz K. Karch, Thomas Ertl
University of Stuttgart, Stuttgart, Germany, e-mail: {sadlo|karchgz|ertl}@visus.uni-stuttgart.de

extraction of topological structures from time-dependent vector fields. The separatrices no longer provide information on the true transport of massless particles, since stream lines (or stream surfaces in 3D) only capture the instantaneous structure of the field. Thus, an alternative approach has recently gained importance that obtains a time-dependent counterpart to separatrices called Lagrangian coherent structures (LCS). The LCS represent transport barriers in time-dependent flow and can be obtained as ridges of the finite-time Lyapunov exponent (FTLE) [7], which measures the separation of neighboring particles as they are advected by the flow. This approach allows for qualitative analysis of time-dependent flows, as the LCS separate regions of different behavior over time.

So far, however, only advective transport has been taken into account in topology-based flow visualization, neglecting additional mechanisms that can cause transport, such as diffusion. Diffusion is present in a wide range of physical and mathematical processes including flows, where it leads to advection-diffusion flow problems. Traditional LCS computed from the velocity field by means of the FTLE obviously cannot depict the true transport of species of interest, such as temperature or solubles, in time-dependent advection-diffusion flow. These LCS exhibit substantial cross-flux of the species due to the involved diffusion and hence cannot separate regions of qualitatively different advection-diffusion. By including diffusion flux of the quantity under examination into the flow map computation, we obtain FTLE ridges that are consistent with the true transport of the respective quantity in advection-diffusion flow. Beyond the resulting LCS, we also show the utility of combining the velocity field with the involved diffusion fluxes. The resulting advection-diffusion field represents the instantaneous transport of the quantity of interest—and because it represents a vector field, the entire body of literature on flow visualization can be applied to it. We demonstrate this for the example of temperature diffusion (thermal conduction) in flows by extracting, additional to LCS, vortex core lines from this field and by providing respective interpretations.

This chapter is organized as follows: In Sec. 2 we discuss related work. In Sec. 3 we introduce the advection-diffusion field that provides a basis for generic visualization of advection-diffusion processes. Two existing feature extraction techniques are briefly described in Sec. 4, while in Sec. 5 these features are extracted from three advection-diffusion CFD datasets and discussed. Sec. 6 concludes this work.

2 Related Work

Flow visualization by topological features has proven successful in a wide range of applications. The field was founded by the works of Perry and Chong [25], Helman and Hesselink [9, 10], and Globus et al. [5]. About a decade later an increase in research in this field has taken place, in the works of Hauser et al. [18] regarding dynamical systems, and Weinkauf et al. with respect to new topological features—starting with saddle connectors [40], and followed by connectors of boundary switch curves [45]. They also proposed a first approach [41] to topological features that are able to reflect the true transport behavior in time-dependent vector fields—motivated by the incapability of traditional vector field topology in this respect due to its definition by (instantaneous) stream lines. By introducing the concept of the local Lyapunov exponent [19], later called direct Lyapunov exponent by Haller [7], and finally called finite-time Lyapunov exponent (FTLE), into the field of visualization, Garth et al. [4] and Sadlo and Peikert [29] provided a nowadays popular basis for scientific visualization by means of topological features in time-dependent vector fields. As proposed by Haller [7] and subsequently defined by Shadden et al. [36], the local maximizing curves in the FTLE field, called Lagrangian coherent structures (LCS), represent a time-dependent counterpart to separatrices. Several (and even contradicting) definitions for these curves have been proposed by Haller [7], Shadden et al. [36], and others. In the field of visualization, Sadlo and Peikert [29, 28] proposed the extraction of LCS by means of height ridges [2].

It has to be noted that FTLE ridges can fail to represent LCS due to two reasons: insufficient advection time [36, 30] or shear. More recently, Sadlo and Weiskopf [31] have generalized 2D vector field topology to time-dependent vector fields by replacing the role of stream lines by streak lines in the concept, and Üffinger et al. [44] have extended this approach to 3D. It is worth noticing that these approaches (and the recent work by Haller [8]) obtain only LCS caused by hyperbolic mechanisms—avoiding those caused by shear flow which do not necessarily represent transport barriers even if long advection times are used for the FTLE computation (resulting in sharp ridges). We refer the reader to the state of the art report by Pobitzer et al. [26] for further details on topology-based visualization in time-dependent vector fields. The FTLE has further been extended to tensor fields by Tricoche et al. [43] and Hlawatsch et al. [11]. Furthermore, it has been applied to a wide range of problems including video analysis by Kuhn et al. [16]. More recently the FTLE has been extended to uncertain vector fields by Schneider et al. [35], while Otto et al. [20] extended the traditional instantaneous vector field topology to uncertain vector fields.

Further works beyond hyperbolic topological structures include those focusing on critical point analogues by Kasten et al. [15] and Fuchs et al. [3], and those by Peikert and Sadlo [22, 23, 24] to reveal the structure in recirculating flow, in particular vortex breakdown bubbles. These have been followed up by techniques due to Tricoche et al. [42] and Sanderson et al. [32] for visualizing the structure of the recurrent magnetic field in Tokamak fusion reactors. More recently, [34] applied FTLE ridges for analyzing the air flow in revolving doors. In contrast to our results, [34] reports only a very loose relation between FTLE ridges and temperature, possibly because thermal conduction (numerical diffusion in the solver) or sub-scale mixing due to turbulence was not taken into account.

Only few works have so far been presented related to advection-diffusion flow. The most closely related work is by Karch et al. [14], where we present an interactive dye advection technique that can take into account diffusion fluxes, i.e., can move the virtual dye according to the true advection-diffusion transport of quantities. Other works have made use of diffusion-related concepts for visualizing advection-only flow, such as the reaction-diffusion technique by Sanderson et al. [33], or the anisotropic diffusion approach by Bürkle et al. [1].

3 Advection-Diffusion Field

In [14] we achieved a visualization of the transport of quantities in advection-diffusion flow by moving virtual dye according to the combination of advective fluxes (i.e., the velocity field) and diffusion fluxes. While we formulated the dye advection by means of the finite volume method, i.e., in terms of fluxes at the boundaries of each sampling cell, we derive here the so-called *advection-diffusion field*, a vector field describing the true transport of the respective quantity, such as temperature or solubles, due to advection-diffusion.

The advection-diffusion vector field is derived from the dye advection formulation [14] as follows. Pure advection of the virtual dye concentration $\phi = \phi(\mathbf{x},t)$ with respect to the simulated velocity field $\mathbf{u} = \mathbf{u}(\mathbf{x},t)$ is modeled by

$$\frac{\partial \phi}{\partial t} + (\nabla \phi)\mathbf{u} = 0.$$

Including *passive diffusion*, i.e., the motion of the dye with respect to the diffusion fluxes of the simulated quantity $\psi = \psi(\mathbf{x},t)$, such as temperature or a soluble, with its constant of diffusivity D_ψ, according to Fick's law of diffusion, reads

$$\frac{\partial \phi}{\partial t} + (\nabla \phi)\mathbf{u} = (\nabla \phi) D_\psi \nabla \psi$$

and leads to equation 7 from [14]

$$\frac{\partial \phi}{\partial t} + (\nabla \phi)(\mathbf{u} - D_\psi \nabla \psi) = 0.$$

This represents again a pure advection problem, however, now with respect to the advection-diffusion field

$$\mathbf{u}_\psi = \mathbf{u} - D_\psi \nabla \psi. \tag{1}$$

Hence, $\mathbf{u}_\psi$ describes the transport of the quantity ψ by means of advection-diffusion. Since $\mathbf{u}_\psi$ represents a vector field, all techniques from flow visualization can be applied to it, however, with the difference that they then reveal the transport of ψ with respect to advection-diffusion, instead of the transport of massless particles due to $\mathbf{u}$, as in the majority of traditional flow visualization.

In this work we present the extraction of topological features from $\mathbf{u}_\psi$ and show how they can be interpreted. The contribution of this chapter is not in terms of techniques for the extraction of topological features per se, but the introduction of the advection-diffusion field and in particular the application of topological feature extraction to this field. To the best of our knowledge, there has not been any work on the visualization of features in advection-diffusion flow yet, and due to the wide presence of advection-diffusion problems and the importance of the visualization of the involved transport of quantities, we see this as an important contribution to the field of scientific visualization. The extraction of LCS, for example, enables answering questions such as where heat is transported from by advection-diffusion—

since the LCS represent transport barriers with respect to advection-diffusion. While the potential of visualization by LCS from $\mathbf{u}_\psi$ is evident, we also provide examples how the topology-related concept of vortex core lines in $\mathbf{u}_\psi$ can provide insight into the transport behavior of the quantity under examination.

The advection-diffusion field $\mathbf{u}_\psi(\mathbf{x})$ can either be computed on the fly during visualization, i.e., $\mathbf{u}(\mathbf{x})$ and $\nabla\psi(\mathbf{x})$ can be interpolated/evaluated at required positions $\mathbf{x}$ and then combined according to Eq. 1, or it can be precomputed at the nodes of the simulation grid and directly fed into existing visualization algorithms. In this work we follow the latter approach since interchanging interpolation and, e.g., multiplication is a common approach in visualization, in particular in feature extraction (see, e.g., [39]). However, it has to be noted that it introduces (typically negligible) error, which did not represent a problem in our experiments. We estimate the gradient $\nabla\psi(\mathbf{x})$ using least squares fitting according to [28]. Note that the constant of diffusivity D_ψ that was used in the CFD simulation has to be available for visualization, however, it is typically uniform and hence only a single number.

4 Feature Extraction

We exemplify feature extraction from the advection-diffusion field $\mathbf{u}_\psi$ using LCS by means of FTLE ridges (Sec. 4.1) and vortex core lines (Sec. 4.2). In Sec. 5 we present the results obtained from applying the feature extraction techniques to three CFD results of advection-diffusion flow.

4.1 Lagrangian Coherent Structures

Lagrangian coherent structures serve as a replacement for separatrices from traditional vector field topology, with the important difference that they are able to correctly depict transport in time-dependent vector fields. Several—and even contradicting—definitions for coherent structures exist. Hussain [12] defined them in terms of the curl of the velocity field, while Robinson [27] provided a more general definition based on correlation of flow variables—both defining coherent structures as volumes in 3D vector fields. In contrast, in the definitions of Haller [6] and Ide et al. [13], Lagrangian coherent structures represent the counterpart to invariant manifolds, i.e., they separate regions of qualitatively different behavior. As discussed in Sec. 2 it was proposed by Haller [7] and subsequently defined by Shadden et al. [36] that ridges in the finite-time Lyapunov exponent (FTLE) field represent LCS. In this work we follow the approach by Sadlo and Peikert [28] and extract LCS from the FTLE field by means of height ridges [2]. To assure sufficiently sharp ridges—according to Shadden et al. [36] a prerequisite for FTLE ridges to represent LCS—we reject ridge regions where the modulus of the respective eigenvalue of the FTLE Hessian is too small or where the FTLE value itself does not reach a user-defined threshold. Due to space limitations, we refer the reader to [28] for all details of our LCS extraction.

The FTLE is a scalar field that describes the separation of neighboring trajectories after a finite advection time interval T. The FTLE at point $\mathbf{x}$ and time t_0 with respect to the time interval T reads

$$\sigma(\mathbf{x}, t_0, T) = \frac{1}{|T|}\sqrt{\lambda_{\max}\left((\nabla\phi_{t_0}^{t_0+T}(\mathbf{x}))^\top \nabla\phi_{t_0}^{t_0+T}(\mathbf{x})\right)}$$

where $\sqrt{\lambda_{\max}(\cdot)}$ represents the spectral norm $\|\cdot\|$ of a matrix with $\lambda_{\max}(\mathbf{A})$ being the major eigenvalue of matrix $\mathbf{A}$. $\nabla\phi_{t_0}^{t_0+T}(\mathbf{x})$ is the gradient of flow map $\phi_{t_0}^{t_0+T}(\mathbf{x})$ which maps starting points $\mathbf{x}(t_0)$ of trajectories to their end points at time $t_0 + T$:

$$\phi_{t_0}^{t_0+T}(\mathbf{x}) = \mathbf{x}(t_0) + \int_{t_0}^{t_0+T} \mathbf{u}(\mathbf{x}(\tau), \tau)\,\mathrm{d}\tau.$$

Depending on the sign of T, i.e., if forward or reverse trajectories are used for the computation of the FTLE, the FTLE ridges represent either repelling ($T > 0$) or attracting ($T < 0$) LCS. We color repelling LCS red and attracting ones blue. It has to be noted that the FTLE field can be sampled independently from the simulation grid on which $\mathbf{u}$, or $\mathbf{u}_\psi$, is given. In this work we use uniform sampling grids, although some of the used advection-diffusion CFD simulations are given on unstructured grids. The integration of the trajectories is accomplished by the 4th-order Runge-Kutta scheme.

4.2 Vortex Core Lines

Vortex core lines—sometimes also denoted as vortex axes—are in close relation to topological features for several reasons. First of all, they are typically identical to critical points of type center and focus in 2D flow. While in 3D the so-called topological vortex cores due to Globus et al. [5] directly represent 1D manifolds of spiral saddle critical points, the relation is less obvious for other definitions of vortex core lines. Since not all vortex core lines represent stream lines, it is nowadays more common to extract them according to the definitions by Levy [17] or Sujudi and Haimes [38]. In this work we use the definition by Sujudi and Haimes, which identifies those points as part of a core line where velocity is parallel or antiparallel to a real eigenvector of the velocity gradient and the other eigenvectors are complex. If the flow is projected on the eigenplane spanned by the complex eigenvectors, this definition corresponds to a critical point of type center or focus in the projected field—further supporting the proximity of vortex core lines and vector field topology. Due to the same reasons, spiral saddle and spiral source critical points typically reside on vortex core lines according to Sujudi and Haimes. As with the other feature extractions, we apply the concept to $\mathbf{u}_\psi$ instead of $\mathbf{u}$ for analyzing the transport of the quantity that is governed by advection-diffusion.

We extract the vortex core lines using the parallel vectors operator due to Peikert and Roth [21], according to their algorithm that triangulates the faces of each cell and solves for the points where the core lines intersect the faces. These points are then connected by piecewise linear segments to obtain the final polyline representation of the core lines.

5 Results

We demonstrate our approach using three advection-diffusion CFD simulations—a static mixer (Sec. 5.1), a flow around a heating coil (Sec. 5.2), and a buoyant flow in a room that is heated at its bottom and cooled at the top (Sec. 5.3). The FTLE field (and its ridges) is computed on a uniform grid in the regions marked by black boxes, while the $\mathbf{u}$ and $\mathbf{u}_\psi$ fields are evaluated at the original grid without resampling.

5.1 Static Mixer

The first simulation is steady-state and was conducted on a unstructured grid consisting of 2266894 tetrahedra. It represents a mixing device that mixes a hot and a cold fluid by means of a strong vortex that is maintained by the tangential inflows. The mixed fluid is provided at an axial outlet at the top, see Fig. 1(a). The upper half of the solid boundary is not visualized to reveal the interior flow—the removed part is illustrated by its edges and a half in wireframe representation. Hot air at 700 K enters at the left lower inlet while cold air at 300 K enters at the lower right inlet.

While in Fig. 1(a) the path lines follow the velocity field $\mathbf{u}$, they follow the advection-diffusion field $\mathbf{u}_\psi$ in Fig. 1(b). It is apparent that the lines of the hot fluid are attracted toward the center (which exhibits average temperature due to mixing) in (b), starting right after they have left the inlet tube. This directly visualizes the transport of heat by advection-diffusion from the left inlet, in contrast to (a) where the lines only show the advection part—using (a) for the interpretation of heat transport would give the wrong picture. Surprisingly, there is an asymmetry with respect to the cold flow in (b). Since there is no negative heat, the blue lines of the cold fluid are not attracted toward the center as they enter the mixer from the right inlet—instead, they are pushed against the outer wall (see that these lines approach the center vortex slower than the blue lines in (a)) because heat from the mixed fluid at the center of the mixer is diffusing into the cold fluid. Hence, the blue lines in (b) depict how heat contained in the cold fluid is transported by advection-diffusion—it is 'avoiding' the heat from the warmer fluid. Because the center of the vortex consists of mixed fluid, there is no detectable deviation between the vortex core line in (a) and (b), i.e., heat is transported there almost purely by advection and therefore the vortex core lines are basically identical.

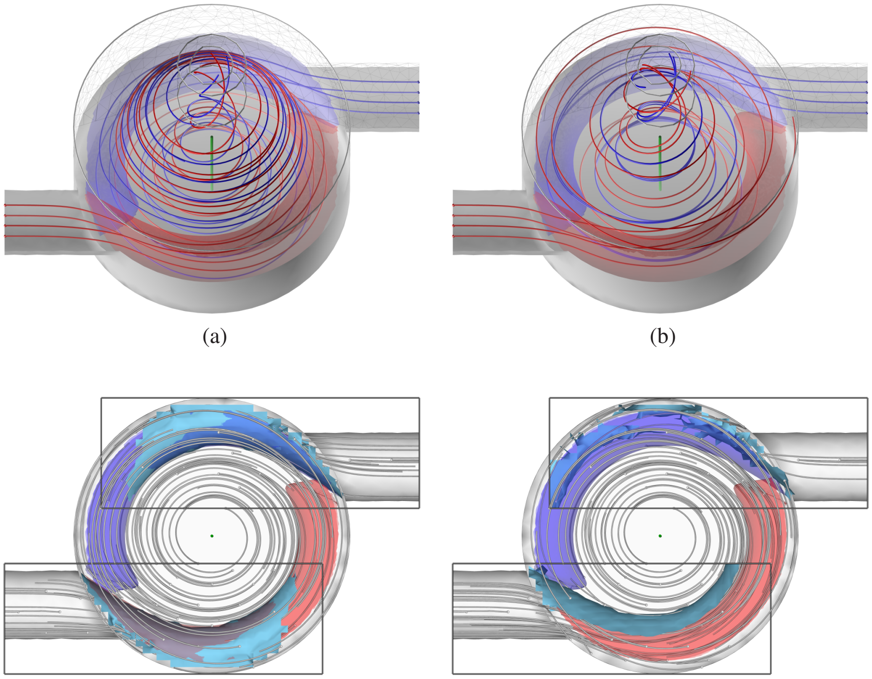

(a) (b)

(c) (d)

Fig. 1 Static Mixer flow example. (a) Visualization of $\mathbf{u}$ (advection only) by path lines (red: hot; blue: cold; seeds by spheres), a vortex core line (green), and two transparent isosurfaces (red: 550 K; blue: 450 K, same in (a)–(d)). (b) Same as (a), but path lines and vortex core line visualizing advection-diffusion field $\mathbf{u}_\psi$. Hot path lines are initially forced toward the center by heat diffusion while blue path lines are initially forced toward the wall due to heat diffusion from the hot flow. (c) Attracting LCS of $\mathbf{u}$ (light blue) are close to the isosurfaces (a subset of respective reverse FTLE trajectories in gray). (d) Attracting LCS of $\mathbf{u}_\psi$ (light blue) depict regions where heat is transported to by advection-diffusion (with a subset of respective reverse FTLE trajectories in gray).

To investigate the transport of heat from the inlets, we have computed LCS using reverse-time FTLE on a regular sampling grid of $17 \times 47 \times 15$ nodes from both the $\mathbf{u}$ (Fig. 1(c)) and $\mathbf{u}_\psi$ (Fig. 1(d)) fields in the regions of interest marked by the black boxes. Consistent with the observations and interpretation so far, the LCS of the hot flow deviates toward the center in (d) while the LCS of the cold flow is attracted toward the wall in (d). The LCS of the hot flow in (d) separates the region (bottom of the image) where heat is transported from the left inlet by advection-diffusion. The LCS of the cold flow in (d) separates the region (top of the image) that does not obtain any heat on its way from the inlet. In contrast, the LCS in (c) are very similar to the isosurfaces. Please note that the isosurface of average temperature (500 K) extends to the center of the mixer in a helical manner.

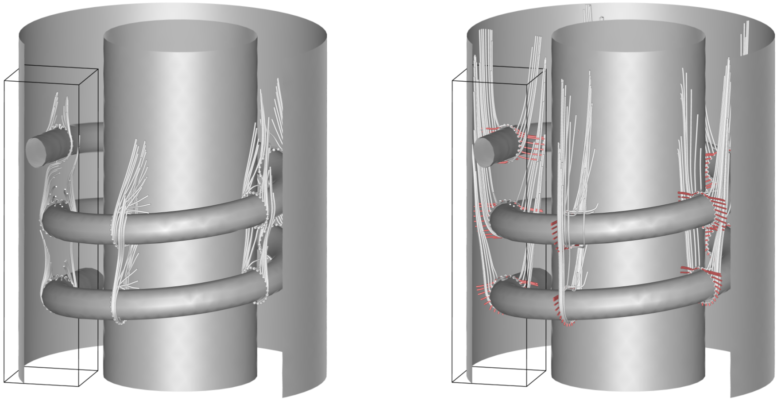

(a) (b)

Fig. 2 Heating Coil flow example. (a) Path lines of $\mathbf{u}$ (white, advection only) seeded at circles around coil (white spheres). (b) Path lines of $\mathbf{u}_\psi$ (white, advection-diffusion) and of $-D_\psi \nabla \psi$ (red, diffusion only). Compared to (a), the white lines in (b) are attracted by the inner and outer wall. This is due to thermal conduction (diffusion of heat) from the heated coil to the cooled walls.

5.2 Heating Coil

This dataset is quasi-stationary and consists of an unstructured grid of 93227 cells, including tetrahedra, pyramids, and prisms. Hence, we used a single time step for a steady-type analysis. The simulation represents a heat exchanger—a heated coil is immersed into an air flow with the inlet at its bottom and the outlet at the top while the inner and outer boundaries (the two vertical tubes) are cooled, see Fig. 2. Buoyant forces have not been employed, resulting in a rather simple flow.

In Fig. 3(c) a subset of the reverse-time trajectories of $\mathbf{u}$ is shown that were used for FTLE computation on a regular grid of $41 \times 41 \times 161$ nodes within the region of interest (ROI, black box). Fig. 3(a) shows some vortex core lines (green) extracted from $\mathbf{u}$ and some stream lines that have been seeded in their vicinity (white tubes). In Figs. 3(b) and (d), the same has been conducted for the advection-diffusion field $\mathbf{u}_\psi$. It is apparent that the vortices along the coil are not present in (b). This is because the transport of heat away from the coil by diffusion (see also stream lines of $-D_\psi \nabla \psi$) is stronger than the advective recirculation at the downstream edge of the coil, resulting in heat transport that has no upstream component. The same can be observed at the top left vortex. It is still present because it is a longitudinal vortex oriented in direction of heat diffusion—however, one can see that the longitudinal component is much stronger with respect to heat transport. Nevertheless, it is an example where heat transport by advection-diffusion exhibits a vortex. The cross sections in Figs. 3(a) and (b) visualize $\nabla \cdot \mathbf{u}$ and $\nabla \cdot \mathbf{u}_\psi$, respectively. The 25th and 75th percentiles of $\nabla \cdot \mathbf{u}_\psi$ are -0.276 and 0.0191, respectively (i.e., rather low compared to $0.05\ \mathrm{m/s}$ average speed and 0.5 m ROI width). The direct impact of $\nabla \cdot \mathbf{u}_\psi$ on LCS (see below) is rather low since $\nabla \cdot \mathbf{u}_\psi$ is substantially smaller at the LCS.

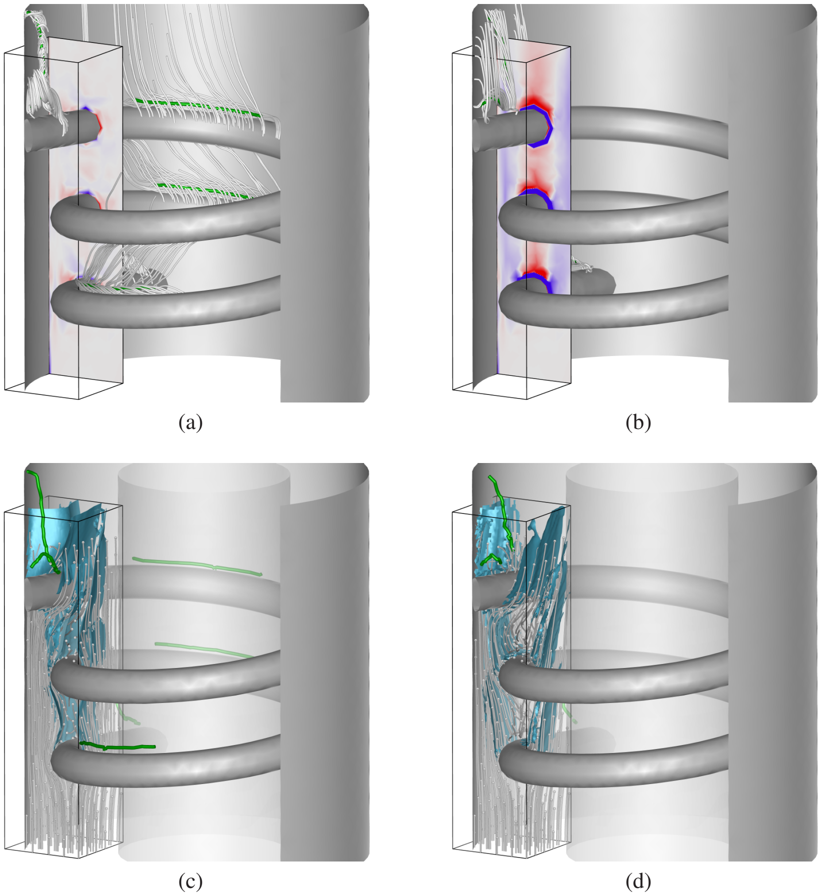

Fig. 3 Heating Coil flow example, region of interest (black box) from Fig. 2. (a) Vortex core lines (green), some forward and reverse stream lines (white) seeded therefrom, and cross section visualizing divergence (red: -0.5, blue: 0.5), all computed from $\mathbf{u}$ (advection only). (b) Same as (a) but computed from advection-diffusion field $\mathbf{u}_\psi$. The strong heat flux from the coil dominates the recirculations at the downstream edge of the coil, hence these vortices disappear. (c) LCS (cyan) from reverse FTLE of $\mathbf{u}$ for comparison with a subset of used trajectories (gray). (d) LCS (cyan) from reverse FTLE of $\mathbf{u}_\psi$ with a subset of used trajectories (gray). It is apparent that in (d) LCS are repelled from the coil due to thermal conduction from the coil to the cooled walls. The LCS separate the region that obtains heat by advection-diffusion from the respective part of the coil.

We investigated the transport of heat from the heating coil by computing LCS from reverse-time FTLE using $\mathbf{u}$ (Fig. 3(c)) and $\mathbf{u}_\psi$ (Fig. 3(d)). It is apparent that in (d) the LCS are repelled from the heating coil toward the inner and outer walls. The LCS region at the lowest turn of the coil in (d) separates the region that is reached by the heat from the coil by means of advection-diffusion. The levels where the LCS reach the inner and outer walls depict the points where heat is transported from the heated coil to the cooled walls.

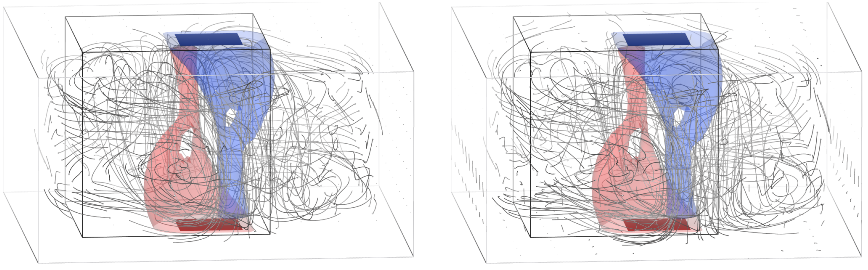

(a) (b)

Fig. 4 Buoyant Flow example at time 24.474 s with transparent isosurfaces (red at 318.5 K; blue at 308.5 K; same as in Fig. 5), region of interest (black) used in Fig. 5, and hot and cold plate. (a) Path lines of $\mathbf{u}$ show advection. (b) Path lines of $\mathbf{u}_\psi$ show transport of heat due to advection-diffusion.

5.3 Buoyant Flow

The final example is a time-dependent simulation of buoyant flow consisting of 2000 time steps simulated on a uniform grid of $60 \times 30 \times 60$ cells. There is a region heated at 348.15 K at its bottom and a cooled region at 278.15 K at its top, and gravity is pointing downward. The rest of the walls are adiabatic. The buoyant flow exhibits transient aperiodic convection, see Fig. 4.

Figure 5(a) shows some of the reverse-time trajectories used for FTLE computation on a regular sampling grid of $41 \times 41 \times 41$ nodes (black box) from $\mathbf{u}$, while (b) shows those computed from the advection-diffusion field $\mathbf{u}_\psi$. It is apparent that many trajectories that show the transport of heat in (b) leave the domain at the hot plate. The reason for this is that heat enters the domain in this region. In (a) there is a vortex of $\mathbf{u}$ (green) located about the center between the cold and hot plumes (visualized by the transparent red and blue isosurfaces). In (b) the vortex of $\mathbf{u}_\psi$ is shifted toward the bottom of the domain and it is intensified (see white stream lines of $\mathbf{u}_\psi$ seeded in its vicinity). Here, the heat flux due to diffusion in the advection-diffusion flow originating at the bottom hot plate rises and then diffuses partially into the cold plume, causing the vortex to shift downward and accelerating the vortex. Such vortices in heat transport can represent undesired configurations in advection-diffusion flow because they can hinder the overall transport of heat.

In Figs. 5(c) and (d) we have computed reverse-time LCS from $\mathbf{u}$ and $\mathbf{u}_\psi$, respectively. In (c) the LCS attaches to the center of the hot plate at the bottom—hence it partially separates the domain in two regions: the region that obtains its flow from the bottom right front corner of the domain and the region that obtains the flow from the bottom left back corner region. In contrast, in (d) the LCS wraps the complete hot flow that is generated by the bottom plate. In other words, the LCS in (c) shows where the flow comes from, while in (d) the LCS shows where the heat comes from—it separates the region that obtains heat from the bottom hot plate by advection-diffusion.

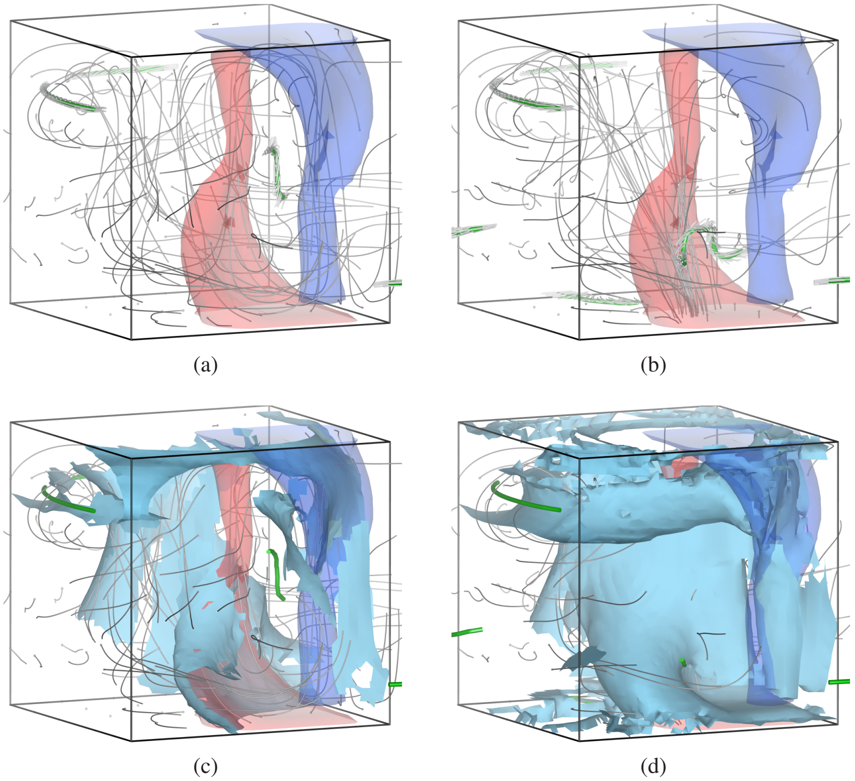

(a) (b)

(c) (d)

Fig. 5 Buoyant flow example. (a) Trajectories in $\mathbf{u}$. (b) Trajectories in $\mathbf{u}_\psi$. (c) Reverse-time LCS in $\mathbf{u}$. (d) Reverse-time LCS in $\mathbf{u}_\psi$ depict region that obtains heat from hot bottom plate.

6 Conclusion

We proposed visualization of the advection-diffusion field, a field that describes the transport of quantities due to advection-diffusion, and presented the extraction of topological features therefrom. These features give valuable insights into transport processes due to advection-diffusion. We applied our approach to three CFD datasets and provided interpretations that gave insight into the underlying phenomena. We believe that visualization by means of topological features in the advection-diffusion field has a high potential in many fields of science and engineering, e.g., in heat exchanger design. As future work, we plan to apply our approach to real-world problems and to extend it to advection-diffusion of vector quantities. Future work could also follow [37] and compare path lines of $\mathbf{u}$ with stream lines of $-D_\psi \nabla \psi$.

Acknowledgements This work was supported by the Cluster of Excellence in Simulation Technology (EXC 310/1) and the Collaborative Research Center SFB-TRR 75 at University of Stuttgart.

References

1. D. Bürkle, T. Preußer, and M. Rumpf. Transport and anisotropic diffusion in time-dependent flow visualization. In *Proc. IEEE Visualization*, pages 61–67, 2001.
2. D. Eberly. *Ridges in Image and Data Analysis. Computational Imaging and Vision.* Kluwer Academic Publishers, 1996.
3. R. Fuchs, J. Kemmler, B. Schindler, F. Sadlo, H. Hauser, and R. Peikert. Toward a Lagrangian vector field topology. *Computer Graphics Forum*, 29(3):1163–1172, 2010.
4. C. Garth, G.-S. Li, X. Tricoche, C. D. Hansen, and H. Hagen. Visualization of coherent structures in transient 2d flows. In *Topology-Based Methods in Visualization II*, pages 1–13. Springer, 2009.
5. A. Globus, C. Levit, and T. Lasinski. A tool for visualizing the topology of three-dimensional vector fields. In *Proc. IEEE Visualization*, pages 33–40, 408, 1991.
6. G. Haller. Finding finite-time invariant manifolds in two-dimensional velocity fields. *Chaos*, 10(1):99–108, 2000.
7. G. Haller. Distinguished material surfaces and coherent structures in three-dimensional fluid flows. *Physica D*, 149(4):248–277, 2001.
8. G. Haller. A variational theory of hyperbolic Lagrangian coherent structures. *Physica D: Nonlinear Phenomena*, 240(7):574–598, 2011.
9. J. Helman and L. Hesselink. Representation and display of vector field topology in fluid flow data sets. *IEEE Computer*, 22(8):27–36, 1989.
10. J. Helman and L. Hesselink. Visualizing vector field topology in fluid flows. *IEEE Computer Graphics and Applications*, 11(3):36–46, 1991.
11. M. Hlawatsch, J. Vollrath, F. Sadlo, and D. Weiskopf. Coherent structures of characteristic curves in symmetric second order tensor fields. *IEEE Trans. Vis. Comput. Graph.*, 17(6):781–794, 2011.
12. F. Hussain. Coherent structures and turbulence. *J. Fluid Mech.*, 173:303–356, 1986.
13. K. Ide, D. Small, and S. Wiggins. Distinguished hyperbolic trajectories in time-dependent fluid flows: analytical and computational approach for velocity fields defined as data sets. *Nonlinear Processes in Geophysics*, 9(3/4):237–263, 2002.
14. G. K. Karch, F. Sadlo, D. Weiskopf, C.-D. Munz, and T. Ertl. Visualization of advection-diffusion in unsteady fluid flow. *Computer Graphics Forum*, 31(3):1105–1114, 2012.
15. J. Kasten, I. Hotz, B. Noack, and H.-C. Hege. On the extraction of long-living features in unsteady fluid flows. In *Topological Methods in Data Analysis and Visualization. Theory, Algorithms, and Applications*, pages 115–126. Springer, 2010.
16. A. Kuhn, T. Senst, I. Keller, T. Sikora, and H. Theisel. A Lagrangian framework for video analytics. In *Proc. IEEE Workshop on Multimedia Signal Processing*, 2012.
17. Y. Levy, D. Degani, and A. Seginer. Graphical visualization of vortical flows by means of helicity. *AIAA*, 28(8):1347–1352, 1990.
18. H. Löffelmann, H. Doleisch, and E. Gröller. Visualizing dynamical systems near critical points. In *Proc. Spring Conference on Computer Graphics and its Applications*, pages 175–184, 1998.
19. E. N. Lorenz. A study of the predictability if a 28-variable atmospheric model. *Tellus*, 17:321–333, 1965.
20. M. Otto, T. Germer, and H. Theisel. Uncertain topology of 3d vector fields. In *Proc. IEEE Pacific Visualization Symposium*, pages 67–74, Hong Kong, China, 2011.
21. R. Peikert and M. Roth. The "parallel vectors" operator – a vector field visualization primitive. In *Proc. IEEE Visualization*, pages 263–270, 1999.
22. R. Peikert and F. Sadlo. Topology-guided visualization of constrained vector fields. In *Topology-Based Methods in Visualization*, pages 21–34. Springer, 2007.
23. R. Peikert and F. Sadlo. Visualization methods for vortex rings and vortex breakdown bubbles. In *Proc. Joint Eurographics / IEEE VGTC conference on Visualization*, pages 211–218, 2007.
24. R. Peikert and F. Sadlo. Flow topology beyond skeletons: Visualization of features in recirculating flow. In *Topology-Based Methods in Visualization II*, pages 145–160. Springer, 2009.

25. A. E. Perry and M. S. Chong. A description of eddying motions and flow patterns using critical-point concepts. *Annual Review of Fluid Mechanics*, 19:125–155, 1987.
26. A. Pobitzer, R. Peikert, R. Fuchs, B. Schindler, A. Kuhn, H. Theisel, K. Matković, and H. Hauser. On the way towards topology-based visualization of unsteady flow – the state of the art. In *Eurographics 2010 State of the Art Reports*, pages 137–154, 2010.
27. S. K. Robinson. Coherent motions in the turbulent boundary layer. *Annu. Rev. Fluid Mech.*, 23:601–639, 1991.
28. F. Sadlo and R. Peikert. Efficient visualization of Lagrangian coherent structures by filtered amr ridge extraction. *IEEE Trans. Vis. Comput. Graph.*, 13(6):1456–1463, 2007.
29. F. Sadlo and R. Peikert. Visualizing Lagrangian coherent structures and comparison to vector field topology. In *Topology-Based Methods in Visualization II*, pages 15–30. Springer, 2009.
30. F. Sadlo, M. Üffinger, T. Ertl, and D. Weiskopf. On the finite-time scope for computing Lagrangian coherent structures from Lyapunov exponents. In *Topological Methods in Data Analysis and Visualization II*, pages 269–281. Springer, 2012.
31. F. Sadlo and D. Weiskopf. Time-dependent 2-d vector field topology: An approach inspired by Lagrangian coherent structures. *Computer Graphics Forum*, 29(1):88–100, 2010.
32. A. Sanderson, G. Chen, X. Tricoche, D. Pugmire, S. Kruger, and J. Breslau. Analysis of recurrent patterns in toroidal magnetic fields. *IEEE Trans. Vis. Comput. Graph.*, 16(6):1431–1440, 2010.
33. A. Sanderson, C. R. Johnson, and R. M. Kirby. Display of vector fields using a reaction-diffusion model. In *Proc. IEEE Visualization*, pages 115–122, 2004.
34. B. Schindler, R. Fuchs, S. Barp, J. Waser, A. Pobitzer, R. Carnecky, K. Matkovic, and R. Peikert. Lagrangian coherent structures for design analysis of revolving doors. *IEEE Trans. Vis. Comput. Graph.*, 18(12):2159–2168, 2012.
35. D. Schneider, J. Fuhrmann, W. Reich, and G. Scheuermann. A variance based ftle-like method for unsteady uncertain vector fields. In *Topological Methods in Data Analysis and Visualization II*, pages 255–268. Springer, 2012.
36. S. C. Shadden, F. Lekien, and J. E. Marsden. Definition and properties of Lagrangian coherent structures from finite-time Lyapunov exponents in two-dimensional aperiodic flows. *Physica D: Nonlinear Phenomena*, 212:271–304, 2005.
37. K. Shi, H. Theisel, H. Hauser, T. Weinkauf, K. Matkovic, H.-C. Hege, and H.-P. Seidel. Path line attributes - an information visualization approach to analyzing the dynamic behavior of 3D time-dependent flow fields. In *Topology-Based Methods in Visualization II*, pages 75–88. Springer, 2009.
38. D. Sujudi and R. Haimes. Identification of swirling flow in 3d vector fields. In *Proc. 12th AIAA Computational Fluid Dynamics Conference*, pages 95–1715, 1995.
39. H. Theisel, J. Sahner, T. Weinkauf, H.-C. Hege, and H.-P. Seidel. Extraction of parallel vector surfaces in 3D time-dependent fields and application to vortex core line tracking. In *Proc. IEEE Visualization*, pages 631–638, 2005.
40. H. Theisel, T. Weinkauf, H.-C. Hege, and H.-P. Seidel. Saddle connectors - an approach to visualizing the topological skeleton of complex 3d vector fields. In *Proc. IEEE Visualization*, pages 225–232, 2003.
41. H. Theisel, T. Weinkauf, H.-C. Hege, and H.-P. Seidel. Stream line and path line oriented topology for 2d time-dependent vector fields. In *Proc. IEEE Visualization*, pages 321–328, 2004.
42. X. Tricoche, C. Garth, A. Sanderson, and K. Joy. Visualizing invariant manifolds in area-preserving maps. In *Topological Methods in Data Analysis and Visualization II*, pages 109–124. Springer, 2012.
43. X. Tricoche, M. Hlawitschka, S. Barakat, and C. Garth. Beyond topology: A Lagrangian metaphor to visualize the structure of 3d tensor fields. In *New Developments in the Visualization and Processing of Tensor Fields*, 2012.
44. M. Üffinger, F. Sadlo, and T. Ertl. A time-dependent vector field topology based on streak surfaces. *IEEE Trans. Vis. Comput. Graph.*, 19(3):379–392, 2013.
45. T. Weinkauf, H. Theisel, H.-C. Hege, and H.-P. Seidel. Boundary switch connectors for topological visualization of complex 3D vector fields. In *Proc. VisSym*, pages 183–192, 2004.